Study of thick active region in a terahertz quantum-cascade laser

Rajesh Sharma*

Department of Pure and Applied Physics, Guru Ghasidas Vishwavidyalaya (A Central University), Bilaspur, Chhattisgarh, India

The research in the area of terahertz (THz) radiation is a subject of intense discussion in the international scientific community owing to its various applications in the fields of defense systems, security, interstellar studies, imaging, and agriculture. Although most of these applications have captured the attention of researchers in recent years, the development of a THz radiation source that meets specific requirements remains a challenging task. In this regard, the emission frequencies of terahertz quantum-cascade lasers (THz QCLs) can be fine-tuned by adjusting the thickness of the quantum well and the height of the barriers. The electron distribution among three periods of a hybrid active region design QCL structure is numerically simulated to estimate the optical gain spectra and electric field strength values. The results of the numerical simulations are compared with those of the experimental investigations by fabricating a $23\,\mu m$-thick active region THz QCL wafer by using the molecular beam epitaxy (MBE) technique. The wafer is split into six portions (A−F) to investigate the transport and the lasing properties. The electrical power dissipated at 10 K for the $23\,\mu m$-thick active region THz QCL stripe processed from the central portion (B) of the wafer is found to be approximately 56 W at the current density value of 0.53 kAcm^{-2}. The thick active region THz QCL investigated in the present work operates in both pulsed and continuous-wave modes at the desired emission frequencies, which is a unique feature of the interlaced design. The optical output power of the $23\,\mu m$-thick active region THz QCL stripe compared to the $12\,\mu m$-thick active region is enhanced, attributed to improved mode confinement. Therefore, optimal performance in the pulsed mode can be achieved with thick active region THz QCL stripes fabricated near the center of the parent wafer. Nevertheless, thin active region THz QCLs are more suitable for continuous-wave operation due to reduced heat dissipation.

KEYWORDS

thick active region, transport and lasing characteristics, terahertz quantum-cascade lasers, quantum wells and barriers, optical gain

1 Introduction

Terahertz quantum-cascade lasers (THz QCLs) are semiconductor lasers which can produce lasing action by using the intersub-band transitions within the heterostructure of quantum wells and barriers [(Williams, 2007; Vitiello et al., 2012; Sharma et al., 2021; Xu et al., 2007; Lee et al., 2010; Amanti et al., 2009; Benz et al., 2009; Qin et al., 2009; Mahler et al., 2010; Barbieri et al., 2004; Williams et al., 2006; Wienold et al., 2010; Jirauschek, 2010; Schrottke et al., 2010)]. The main emphasis of the researchers was to put forward significant efforts to obtain low threshold current density values, high temperature operation, stable emission frequencies, and high optical output powers of THz QCLs. Many researchers have

devoted efforts to increase the efficiency of THz sources [(Terazzi and Faist, 2010; Strupiechonski et al., 2011; Sirtori et al., 1998; Gmachl et al., 2001; Lu et al., 2006; Sharma et al., 2011; Han et al., 2018; Kainz et al., 2018; Albo et al., 2019; Chassagneux et al., 2007; Röben et al., 2021; Hempel et al., 2016; Röben et al., 2019; Li et al., 2014)]. Fathololoumi et al. investigated the THz QCL structures and obtained an operating temperature of 200 K in the pulsed-wave mode operation (Fathololoumi et al., 2012). After this, the scientific community had accelerated the research efforts to obtain higher operating temperatures in the pulsed- and the continuous-wave (CW) mode operation of THz QCLs; however, the researchers were not able to achieve any significant increase in the operating temperature for many years. It was reported that two-quantum well active region design and selection of a special Cu–Cu waveguide can elevate the operating temperature to 210.5 K in the pulsed-wave mode (Bosco et al., 2019). The non-equilibrium Green's function model was applied to optimize the THz QCL structure.

The maximum operating temperature in the pulsed-mode operation of THz QCLs was recently demonstrated to be 250 K at 4 THz by use of a clean n-level system of the active region, where n is the number of upper sub-bands responsible for the lasing action (Khalatpour et al., 2021). The threshold and maximum current density values are found to be 1.54 and 2.60 kA cm^{-2}, respectively. The emission spectra of the single-stage thermoelectric cooled laser were recorded by using a pyroelectric detector (Khalatpour et al., 2021). In 2023, Khatalpour et al. reported the operating temperature of the THz QCL to be 261 K (Khalatpour et al., 2023). It is interesting to note that modeling the THz QCL structure is essential for optimizing device performance. Although a higher operating temperature is obtained in the recent reports (Khalatpour et al., 2023; Gao et al., 2023; Chen et al., 2024; Levy et al., 2024), a high threshold current density value is required to overcome the losses in the optical resonator, which makes it difficult to operate the THz QCL in the CW mode. The highest operating temperature of a CW-mode THz QCL with observable optical output power is 129 K, as reported by Wienold et al. (2014). A more recent study also reports achieving the same operating temperature of 129 K with an output power of 0.3 W (Curwen et al., 2021).

The optical output power of the THz QCL devices can be improved in the pulsed and the CW operation mode by varying the active region thickness, which was explored to some extent in the recent reports of the literature (Brandstetter et al., 2013; Li et al., 2017; Salih et al., 2013). The variation in the active region thickness was investigated for three-well, resonant-phonon depopulation THz QCLs with semi-insulating surface-plasmon waveguide (Salih et al., 2013). The operating parameters of THz QCLs with active-region thicknesses of 10, 7.5, 6, and 5 μm were investigated, and the sample with a 7.5-μm-thick active region was found to attain the best performance (Salih et al., 2013). On the other hand, thickness increases beyond the 10 μm-thick active region THz QCLs were also explored by the scientific community. Consequently, the researchers have tried to increase the output power of the THz QCLs by bonding the wafers of two symmetric active regions (Brandstetter et al., 2013). The optical output power and the maximum operating temperature values were found to be 470 mW at 5 K and 122 K, respectively. The range of the emission frequencies of the THz QCL was approximately 420 GHz, centered at

approximately 3.9 THz. The wafer bonding process requires symmetric wafers and expertise.

In another report, 24 μm-thick active region THz QCLs with a facet coated with high-reflectivity layers was demonstrated to produce 2.4 W optical output power in the pulsed-mode operation at an emission frequency of approximately 4.4 THz at a temperature of 10 K (Li et al., 2017). Although the high optical output power in the pulsed-mode operation of 24 μm-thick active region THz QCLs was observed in the report by Li et al., the electrical power dissipated causes thermal failure if these THz QCLs (Li et al., 2017) are driven in the continuous-wave operation mode. In the case of continuous-wave THz QCLs based on a hybrid bound-to-bound quantum design, the dissipated power ≤30 W has been reported for an active region thickness of approximately 19 μm by Li et al. (Li et al., 2022). Moreover, the investigation of inhomogeneity during the fabrication and schematic processing of the stripes from the central slot to the edge slot of the wafer of the thick active region THz QCLs are still necessary.

In the present article, the threshold optical gain and the optical confinement factor are calculated as a function of the active region thickness, which is followed by numerical simulations to deduce the energy sub-band structure diagram of the GaAs/AlGaAs heterostructure. The optical gain spectra and electric field strength of THz QCLs with the interlaced active regions are estimated by using the self-consistent numerical solutions of the Schrödinger and Poisson equations. As far as the experimental investigations are concerned, we fabricate a 23 μm-thick active region THz QCL wafer in a single-growth run by using the molecular beam epitaxy technique (MBE). The wafer is split into six portions to schematically investigate the transport and lasing characteristics from the center slot to the edge slot. The letters A, B, C, D, E and F only indicate randomly selected portions and different processing runs. Different slots of one of the portions (B) of the parent wafer are processed for many 23 μm-thick active region THz QCL stripes to investigate the effect of homogeneity during the growth as a function of the distance from the center of the wafer. Moreover, the light–current–voltage (LIV) and emission spectra measurements of approximately 14 such THz QCL stripes are investigated from the six portions of the parent wafer where the active region thickness is 23 μm and 12/10 μm.

2 Simulations of transport and lasing characteristics

The threshold optical gain (g_{th}) and the optical confinement factor (Γ) are illustrated by Figure 1a as a function of the active region thickness (Kohen et al., 2005). It is quite evident that the threshold optical gain is high for smaller active region thicknesses, while the optical confinement factor has low values. The optical confinement factor increases with the increase in the active region thickness; however, the threshold optical gain is reduced. The threshold deriving electric power estimated for the 0.75 mm, 1.00 mm, and infinite long ridge lengths is highlighted in Figure 1b. The parameters used to estimate the threshold deriving electric power are wavenumber ($\tilde{\nu}$); electric field; series resistance having values of 158 cm^{-1}, 3.3 kV/cm, and 0.75 Ω,
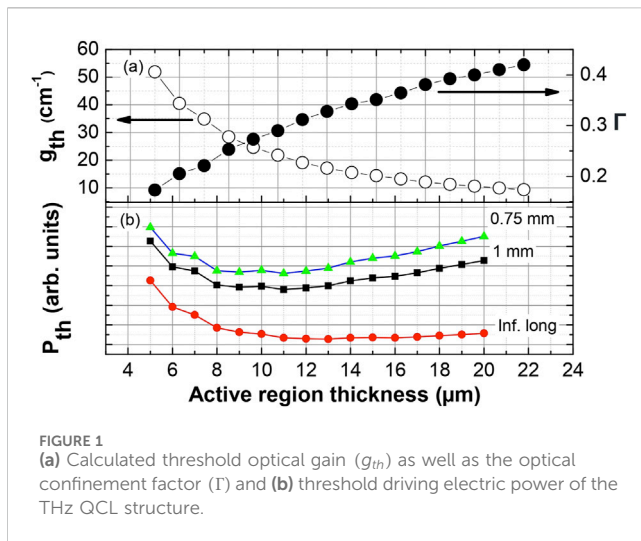
FIGURE 1
(a) Calculated threshold optical gain (g_{th}) as well as the optical confinement factor (Γ) and **(b)** threshold driving electric power of the THz QCL structure.
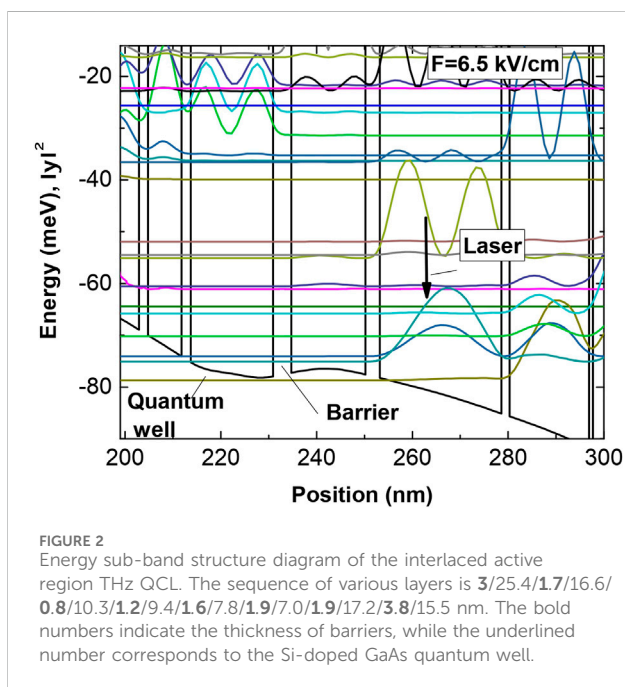

FIGURE 2
Energy sub-band structure diagram of the interlaced active region THz QCL. The sequence of various layers is **3**/25.4/**1.7**/16.6/**0.8**/10.3/**1.2**/9.4/**1.6**/7.8/**1.9**/7.0/**1.9**/17.2/**3.8**/15.5 nm. The bold numbers indicate the thickness of barriers, while the underlined number corresponds to the Si-doped GaAs quantum well.

respectively; and $J_{th} \sim g_{th}$. The threshold optical gain is higher for smaller active region thicknesses in the THz QCL due to the limited amplification region and increased cavity losses. At lower active region thicknesses, the optical confinement factor is also low because of the reduced mode overlap. As the active region thickness increases, there is an enhancement in optical confinement factor; however, the threshold optical gain correspondingly decreases. The energy sub-band structure diagram of the interlaced active region THz QCLs at a field strength of 6.5 kV/cm is depicted in Figure 2 where the vertical laser transition occurs in the same quantum well. In the interlaced active region of the THz QCL, the lower laser level is depopulated through phonon-assisted transitions, while the upper laser level can either be the miniband or a bound state. In normal situations, the layer structure is engineered in such a way that the longitudinal optical phonon emission depopulates the lower laser

level. Designs involving photon emission followed by the phonon emission are also called hybrid designs. The numerical simulations are carried out on the basis of the theoretical details reported in Schrottke et al. (2010), where three periods of the QCL structure are taken into account for the electron distribution.

Figure 3 shows images of the THz QCL stripe processed at a distance of 11.6 mm from the center of the wafer with a ridge width of 200 μm and length of 3413 μm. Figure 3a illustrates a scanning electron microscope image of the THz QCL stripe while Figure 3b shows an image of one portion of length of the wire bonded stripe recorded by using an optical microscope. Note that the total length of the stripe is 3413 μm. The images are taken from portion B of the 23 μm-thick active region wafer.

The outcome of the numerical computation is depicted in Figure 4 where the variations in the electric field strength as a function of the frequency and current density are highlighted. It is to be noted that the maximum value in the optical gain occurs from 4.06 to 5.02 THz, which is illustrated by the vertical dashed lines in Figure 4a. Nevertheless, the onset of the negative differential conductivity (NDC) in Figure 4b is marked by the horizontal dashed line at 6.7 kV/cm and the current density of 517 A cm^{-2}. The electric field increases with increasing current density due to enhanced carrier mobility. However, with a further increase in the current density, carriers transition from the Γ-valley to the L-valley, leading to negative differential conductivity (NDC). The THz QCL turns off at the onset of NDC, which is a well-known issue in GaAs/AlGaAs heterostructures.

3 Experimental configurations

The standard 23 μm-thick active region THz QCL sample is fabricated by using the MBE technique on a semi-insulating GaAs substrate, which is further processed into single-plasmon waveguides. The details of fabrication, processing, and experimental configuration utilized for recording LIV and emission spectra measurements are already reported in our publications (Sharma et al., 2011; Sharma et al., 2013; Wienold et al., 2012; Wienold et al., 2014). Owing to the rotation during the growth procedure in the MBE machine, the THz QCL wafer has a radial symmetry and a negative thickness gradient of approximately 1 to 3% from the central portion to the edge of the wafer. After the fabrication, the parent THz QCL wafer is split into six pieces, i.e., A, B, C, D, E and F, which are further processed to produce several THz QCL stripes. The details of different wafers are highlighted in Table 1 and discussed later in Section 4.

4 Experimental results and discussion

A THz QCL stripe of dimensions 200 × 3555 μm processed from a slot of the wafer portion A is characterized in the pulsed mode, which has shown the output optical power of 4.3 mW and the threshold current density of 475 A cm^{-2} at 5 K. The THz QCL stripe has shown lasing up to a temperature of 45 K. The emission frequencies of the THz QCL are in the range of 5.15–5.23 THz.

In order to understand the growth homogeneity of the fabricated wafers, we have thoroughly investigated portion B of the parent
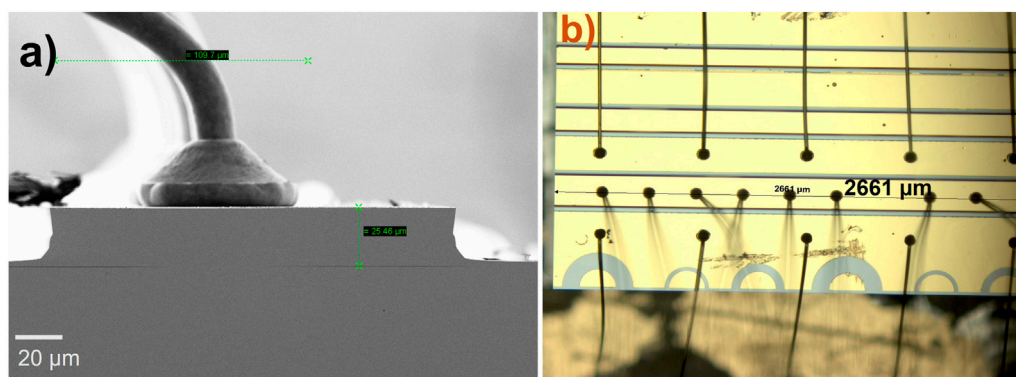
FIGURE 3
Images of the THz QCL stripe processed at a distance of 11.6 mm from the center of wafer with a ridge width of 200 μm and length of 3413 μm. **(a)** Scanning electron microscope image; **(b)** image of one portion of the length of the wire bonded stripe recorded by using an optical microscope. The images are taken from portion B of the 23 μm-thick active region wafer.
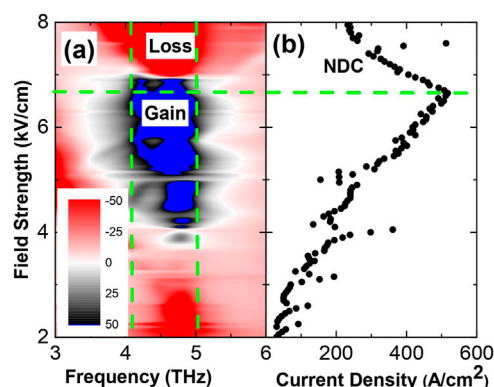

FIGURE 4
Calculated **(a)** optical gain spectra and field strength values of the THz QCL structure with the interlaced active region design. The vertical dashed lines indicate the optical gain region from 4.06 to 5.02 THz. **(b)** The electric field strength profile where the horizontal dashed line indicates triggering of negative differential conductivity (NDC) of the THz QCL structure.

wafer by processing approximately 5 THz QCL stripes from the center to the edge of the wafer. The experimental light–current density–voltage curves of the 23 μm-thick active region THz QCL stripes processed from different parts of the wafer (portion B from the parent wafer) at 5 K temperature are illustrated in Figure 5.

All of the QCL stripes are 200 μm wide, while the lengths are 3.41, 3.40, 3.44, 3.45, and 3.46 mm, respectively, for the THz QCL wafers processed at distances of 11.6 mm, 13.0 mm, 15.4 mm, 17.4 mm, and 19.3 mm, respectively, from the center to the edge of the wafer. The threshold current density values are 258, 311, 366, 454, and 608 A cm^{-2} for the QCL wafers processed at distances of 11.6 mm, 13.0 mm, 15.4 mm, 17.4 mm, and 19.3 mm from the center of the wafer, respectively. The optical output power is found to be 57.3, 31.1, 28.4, 18.4, and 3.1 mW for the QCL stripes processed at distances of 11.6 mm, 13.0 mm, 15.4 mm, 17.4 mm, and 19.3 mm

from the center slot to the edge of the wafer, respectively. Moreover, there is a general trend of smaller voltages (Figure 5) for the THz QCL sample from the center to the edge of wafer. The enhancement in the threshold current density of the QCL stripes from the central slot to the edge of the wafer is consistent with the decrease in the optical output power. The average period length variation from the center to the edge of the THz QCL wafer is found to be 1.5% at a distance of 20 mm from the wafer center. This deviation is not sufficient to explain the increased threshold current density toward the wafer edge.

The elevated threshold current density values can be understood on the basis of increasing interface roughness from the average distance from the center to the edge of the wafer, which can significantly affect the lasing of the THz QCLs (Kumar et al., 2007; Jenichen et al., 1997). The temperature gradient, growth rate modulation, and rotation of the wafers during the growth procedure are possible reasons for increased interface roughness toward the edge of the wafer. Surface roughness of the wafer is not so critical; however, interface roughness can significantly influence the emission frequencies of THz QCLs. This effect can be attributed to composition grading at the interfaces between the quantum wells and barriers in the wafer (Sharma et al., 2013). A strong decrease in the optical output power of the THz QCLs processed away from the central slot to the edge of the wafer can be explained by a significant inhomogeneity in the growth direction. The performance of 23 μm-thick active region QCL stripes is degraded for the laser ridges processed at 11.6 mm distance from the central slot of the wafer.

As found in the inset of Figure 5, the electrical power dissipated for the THz QCL stripe processed at the distance of 11.6 mm from the center to the edge of the wafer at 10 K is found to be approximately 56 W at the current density value of 0.53 kAcm^{-2}. We believe that the thick active region THz QCLs are suitable for obtaining the highest power in the pulsed-mode operation, as investigated in this study and also in the reports of the literature. However, for the continuous-wave operation mode, the THz QCL fabricated in the present

TABLE 1 Details of the different portions of THz QCLs from the parent wafer. Here E_{NDC} is the electric field at the onset of the negative differential conductivity, and AR refers to the active region.

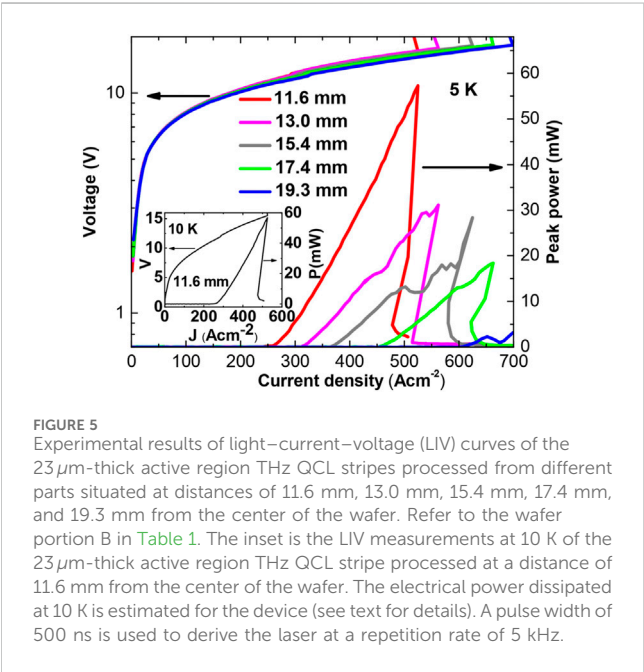| S. N	Wafer portion	AR thickness (μm)	Number of stripes tested	Transport recorded	Lasing recorded	E_{NDC} (kV/cm)
1	A	23	1	Yes	Yes	7.2
2	B	23	5	Yes	Yes	6.7
3	C	12	2	Yes	No	9.4
4	D	23	2	Yes	No	6.4
5	E	12	3	Yes	Yes	8.4
6	F	10	1	Yes	Yes	8.1

FIGURE 5
Experimental results of light−current−voltage (LIV) curves of the 23 μm-thick active region THz QCL stripes processed from different parts situated at distances of 11.6 mm, 13.0 mm, 15.4 mm, 17.4 mm, and 19.3 mm from the center of the wafer. Refer to the wafer portion B in Table 1. The inset is the LIV measurements at 10 K of the 23 μm-thick active region THz QCL stripe processed at a distance of 11.6 mm from the center of the wafer. The electrical power dissipated at 10 K is estimated for the device (see text for details). A pulse width of 500 ns is used to derive the laser at a repetition rate of 5 kHz.

FIGURE 6
The emission spectra measurements in the pulsed-mode operation for the 23 μm-thick active region THz QCL stripe of dimensions 200 × 3413 μm. This THz QCL stripe slot is processed at a distance of 11.6 mm from the central portion of the wafer (refer to LIV characteristics in Figure 5). At 5 K, the emission spectra are recorded near the threshold, intermediate and maximum values of the current density. Only one emission spectrum is obtained at the maximum operating temperature owing to the smaller dynamic range of the current density values.

investigations coupled with the study of the thin active region may be preferred due to the thermal effects.

The emission spectra of standard 23 μm-thick active region THz QCLs measured in the pulsed-mode operation are illustrated in Figure 6.

The spectral mode emission shown in Figure 6 originates from the Fabry−Perot laser cavity modes. The emission spectra cannot be interpreted as a transition from single-mode to multimode emission due to the limited dynamic range of the current density at elevated temperatures. The spectral broadening is governed by lifetime broadening between the two energy states responsible for lasing, along with an additional broadening factor attributed to the interface roughness. The inhomogeneous broadening of the gain spectrum is influenced by this interface roughness, which can be partially controlled through optimized growth conditions. The internal slope efficiency is affected by the inhomogeneous line broadening of the gain spectrum, which typically determines the threshold and operational current density values (Schrottke et al., 2010). Longitudinal mode shifting is primarily governed by the
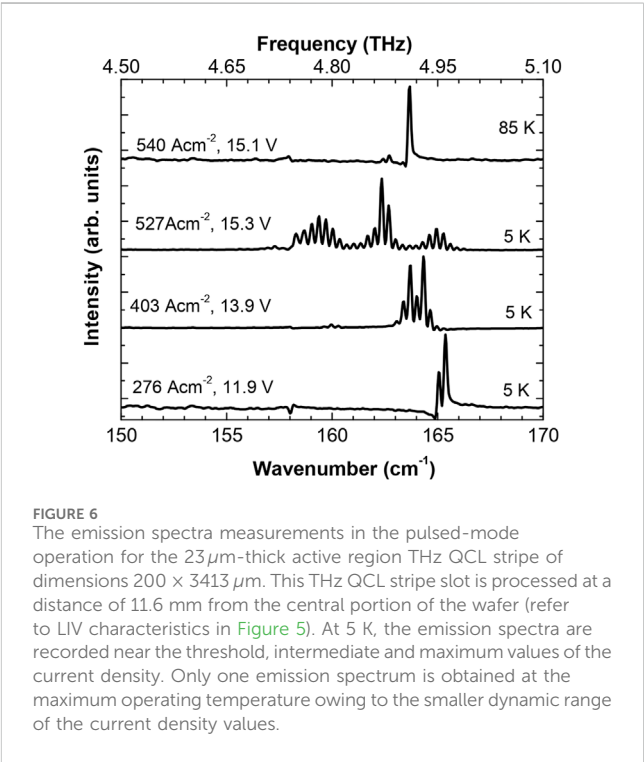
optical gain medium and resonant cavity. These THz QCLs are specifically designed for heterodyne detection and interstellar applications targeting a specific emission frequency of 4.745 THz, where only the central emission frequencies are of significance. For portion B of the parent wafer, the dual mode emission of approximately 4.94 THz is obtained at 5 K at the current density of 276 A cm^{-2}. The relatively broad emission frequency between 4.73 and 4.98 THz is obtained at the current density of 527 A cm^{-2}.

The threshold current density values from the center of wafer are shown in Figure 7A. The maximum and minimum values of the threshold current density are 608 A cm^{-2} and 258 A cm^{-2} at distances of 11.6 and 19.3 mm from the center, respectively. The emission frequencies as a function of distance from the central slot of the wafer are highlighted in Figure 7B. The wide spectrum and blue shift in the emission frequencies from the center slot to the edge slot of the thick active region THz QCL stripe can be explained by
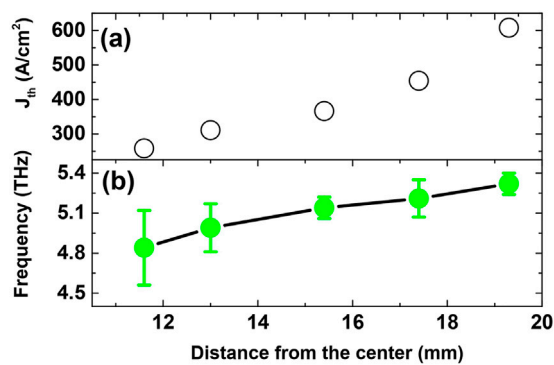
FIGURE 7
(a) The threshold current density and (b) emission frequency values versus distance from the central slot of wafer for 23 µm-thick active region THz QCL.
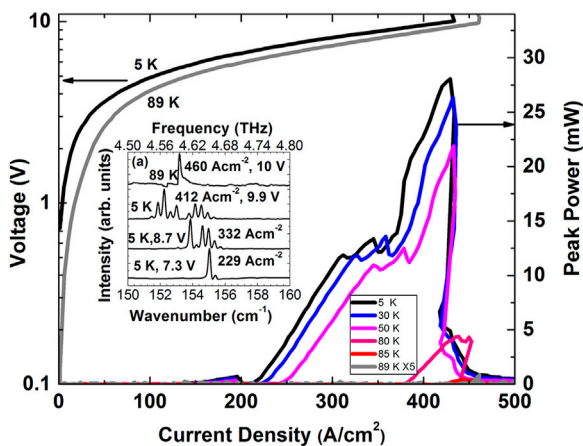

FIGURE 8
The LIV characteristics of 12 µm-thick active region THz QCL stripe with dimensions of 200 × 2925 µm, processed from portion E of the parent wafer. The inset shows the emission spectra measurements at various temperature values. The device is driven in the pulsed operation mode.

homogeneity during the growth of the wafer, which is consistent with recent reports in the literature (Lü et al., 2021). The increase in the threshold current density is attributed to higher effective losses from the center to the edge of the wafer. The emission frequency of the THz QCL depends on the energy difference between subbands, which is directly influenced by the thicknesses of the quantum wells and barriers, as well as the electric field distribution across the device. The observed blue shift in the emission frequencies is attributed to the Stark effect and variations in the thickness of the quantum wells and barriers toward the edge of the wafer.

Portion C of the parent wafer is processed in such a way that only 12 µm of the active region is retained. The transport characteristics of 12 µm-thick active region THz QCL stripes are recorded; however, the device has not shown lasing, which may be due to the inhomogeneities in the growth of THz QCL wafers. We

have also processed and tested two stripes of the THz QCL from portion D of the parent wafer where the transport characteristics are recorded. The investigation of the transport measurements of THz QCL stripes from different portions of the parent wafer are illustrated and discussed at length in the text/caption of Figure 10.

Next, we investigate the LIV and the emission frequency spectra of the THz QCL stripe from portion E of the wafer, which is 200 µm wide and 2.93 mm long. In the pulsed-mode operation, the threshold current density and the optical output power are 140 A cm^{-2} and 28 mW, respectively, as depicted in Figure 8. In the pulsed-mode operation, the emission spectra are recorded and are shown in the inset of Figure 8 where the central emission frequency of 4.66 THz is obtained at the bias voltage of 7.3 V at 5 K. At 8.7 V and 9.9 V, the central emission frequencies are shifted to 4.64 and 4.61 THz at a temperature of 5 K. Since the dynamic range of the applied current densities is limited at the elevated temperature of 89 K, only one emission spectrum could be recorded where the emission frequency is centered at approximately 4.59 THz. In the inset of Figure 8, the emission spectra cannot be interpreted as a transition from single-mode to multimode emission due to the limited dynamic range of current density at the elevated temperature of 89 K. At 5 K, emission spectra are recorded near the threshold, at intermediate, and at maximum current density values. However, at 89 K, only a single emission spectrum is obtained at the maximum current density, owing to the narrower dynamic range. Since the output power at 89 K is significantly lower than that at 5 K, it has been multiplied by a factor of 5 to enhance the visibility—this is a common and accepted practice in QCL literature.

In the next step, we have investigated a 12 µm-thick active region stripe with an intention to operate the device in the pulsed-mode operation and in the CW mode operation. The THz QCL stripe of dimensions 120 × 1205 µm is processed from portion E of the parent wafer. The pulsed-mode operation results of the THz QCL stripe are illustrated in Figure 9a. At 5 K, the threshold current density and optical output power are 230 A cm^{-2} and 3.9 mW, respectively. The limited dynamic range of the current density, J_{max}-J_{th}, is approximately 24 A cm^{-2} which indicate that the higher operating temperature would be difficult to obtain in the case of this stripe. The THz QCL stripe lased up to a temperature of 70 K in the pulsed-mode operation. The same THz QCL stripe of dimensions 120 × 1205 µm is investigated for the LIV measurements in the CW mode operation, and results are depicted in the main panel of Figure 9b. An increase in current density enhances the optical gain of the THz QCL, which saturates at the threshold value. Further increases in the current density lead to higher optical output power. However, electrical power dissipation and thermal effects limit the overall performance of the THz QCL (Kruger et al., 2013). The underlying scattering mechanisms can be understood from Sharma et al. (2021).

At 20 K, the optical output power and threshold current density are 1.3 mW and 318 A cm^{-2}, respectively. The maximum value of the current density at which the device has shown lasing is 484 A cm^{-2}. At 30 K, the optical output power and threshold current density are 0.9 mW and 338 A cm^{-2}, respectively, while the maximum current density is found to be 473 A cm^{-2}. The emission spectra are illustrated in the inset of Figure 9b. At 22 K, 331 A cm^{-2}, 7.3 V, the emission frequency is centered at approximately 4.67 THz, which remains around a similar value
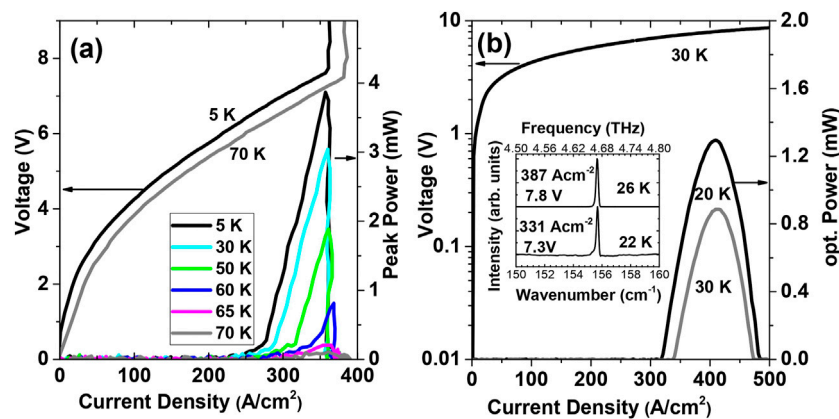
FIGURE 9
(a) The measured LIV curves of the 12 μm-thick active region with the dimensions of 120 × 1210 μm QCL strip, which is processed from portion E of the parent wafer. The device is driven in the pulsed operation mode. **(b)** The CW mode operation LIV characteristics of the 12 μm-thick active region THz QCL stripe with dimensions of 120 × 1210 μm. The inset of **(b)** is the emission spectra measurements in the CW operation mode.
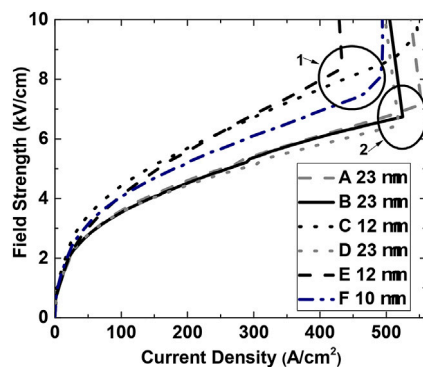

FIGURE 10
The measured electric field strength versus the current density of the THz QCL structures for different portions **(A, B, C, D, E, and F)** of the parent wafer. The circles 1 and 2 indicate 12/10 μm and 23 μm-thick active region THz QCL stripes, respectively.

for 387 A cm^{-2}, 7.8 V at 26 K. This indicates that the output frequency of the THz QCL remains stable in the CW operation mode, although the dynamic range of the current density values is limited.

It is quite obvious from Figure 9b that it is difficult to obtain higher operating temperatures when the device is driven in the CW operation mode because of the thermal effects. It is also reported in the literature that the thicker active region QCL (24 μm) can be exploited for higher optical power in the pulsed mode; however, the thinner active region (5.86 μm) is suitable for the CW operation mode (Chassagneux et al., 2007). The broad surface area stripes are used to obtain the pulsed-mode LIV characteristics of the THz QCLs. Nevertheless, the smaller surface area stripes are preferred for the CW operation of the THz QCL to minimize the effects of thermal heating. The thermal conductance of the THz QCL stripe can be estimated by formula G = (J_{th} V_{th})/ΔT, where J_{th} and V_{th} are the threshold current density and the threshold voltage, respectively. The ΔT is the difference between the pulsed and CW operation

temperature. For J_{th} = 340 Acm^{-2}, V_{th} = 7.4 V, ΔT = 40 K, the thermal conductance value is estimated to be 62.9 W K^{-1}cm^{-2}, which is less compared to our previously investigated devices of epitaxy-up (120 W K^{-1}cm^{-2}) and epitaxy-down (160 W K^{-1}cm^{-2}) mounting schemes (Kruger et al., 2013). In the pulsed-mode operation of the THz QCL, the peak power is calculated by dividing the average power by the duty cycle. In contrast, during the continuous-wave operation, the optical power is directly measured as no pulses are involved. The Y-axis of the emission spectra represents the intensity in arbitrary units. The emission frequency remains unchanged in the continuous-wave operation mode due to the limited dynamic range of the THz QCL under these operating conditions.

The measured electric field strength versus the current density of the THz QCL structures for different portions (A, B, C, D, E, and F) of the parent wafer is illustrated in Figure 10. The circles 1 and 2 represent the onset of the NDC for 12/10 μm and 23 μm-thick active region THz QCL stripes, respectively. The thickness of the active region is 23 μm for the wafer portions A, B, and D.

In the case of the THz QCL stripe processed from portions A and B of the parent wafer, the onset of the NDC occurs at the electric field strength values of 7.2 and 6.7 kV/cm at the maximum current density values of 553 and 524 Acm^{-2}, respectively. On the other hand, the onset of the NDC occurs at the electric field strength of 6.4 kV/cm at the maximum current density value of 519 Acm^{-2} for the THz QCL stripe processed from portion D of the parent wafer. The thickness of the active region is 12 μm for the wafer portions C and E, while the 10 μm-thick active region is retained from portion F of the parent wafer (refer to Table 1).

In the case of the THz QCL stripe processed from portions C and E of the parent wafer, the onset of the NDC occurs at the electric field strength values of 9.4 and 8.4 kV/cm at the maximum current density values of 542 and 433 Acm^{-2}, respectively. Nevertheless, the onset of the NDC occurs at the electric field strength of 8.1 kV/cm at the maximum current density value of 491 Acm^{-2} for the THz QCL stripe processed from portion F of the parent wafer. Carrier injection and energy subband alignment in the THz QCL structure are essential to achieve lasing action. The lasing performance also

depends on the processing conditions of the wafers, which typically determine the measurable optical output power. The electric field strength in wafer C is higher than in the other stripes, and the onset of negative differential conductivity occurs at higher voltages. In contrast, the electric field strength in THz QCL stripes processed from wafer D is lower compared to that of wafer B. As a result, the variation in voltages across wafers C and D in the THz QCL structures leads to reduced optical gain, which in turn limits the optical output power to a measurable level. The onset of negative differential conductivity in THz QCLs depends on the thickness of the active region, the stripe dimensions, and the operating temperature. Circles 1 and 2 represent THz QCL stripes with $12/10\,\mu$m-thick and $23\,\mu$m-thick active regions, respectively. The onset of negative differential conductivity in the $12/10\,\mu$m-thick active region occurs at higher electric field strengths and lower current density values compared to the $23\,\mu$m-thick region. This behavior is attributed to the etching of the top layer. Furthermore, the onset of NDC occurs at a higher voltage at 5 K than at 89 K as additional voltage is required to trigger instabilities at lower temperatures (Figure 8). In contrast, at elevated temperatures, the thermal energy of the carriers combined with the applied voltage is sufficient to reduce the onset voltage.

5 Summary

In summary, we have performed calculations of the threshold optical gain and the optical confinement factor as a function of the active region thickness, which is followed by the numerical simulations to deduce the energy subband structure diagram, the optical gain spectra, and field strength as function of the current density of the THz QCL structure with the interlaced active region design. We have fabricated the $23\,\mu$m-thick active region THz QCL wafer in a single-growth run by using the molecular beam epitaxy technique, which is split into six portions. One of the portion (B) of the parent wafer is processed for many $23\,\mu$m-thick active region THz QCL stripes, where LIV and emission spectra are measured as a function of the distance from the center of wafer. We investigated the light–current–voltage (LIV) and emission spectra measurements of approximately 14 such THz QCL stripes from the six portions of the parent wafer, where the active region thicknesses are $23\,\mu$m, $12\,\mu$m, and $10\,\mu$m. The thick active region THz QCL investigated in the present work operates in both pulsed and continuous-wave modes at the desired emission frequencies, which is a unique feature of the interlaced design. The optical output power of the $23\,\mu$m-thick active region THz QCL stripe shows enhancement compared to the $12\,\mu$m-thick active region, attributed to improved mode confinement. Therefore, optimal performance in the pulsed mode can be achieved with thick active region THz QCL stripes fabricated

near the center of the parent wafer. Nevertheless, thin active region THz QCLs are more suitable for continuous-wave operation due to reduced heat dissipation.

Data availability statement

The raw data supporting the conclusions of this article will be made available by the authors, without undue reservation.

Author contributions

Funding

Acknowledgments

Conflict of interest

The author declares that the research was conducted in the absence of any commercial or financial relationships that could be construed as a potential conflict of interest.

Publisher's note

All claims expressed in this article are solely those of the authors and do not necessarily represent those of their affiliated organizations, or those of the publisher, the editors and the reviewers. Any product that may be evaluated in this article, or claim that may be made by its manufacturer, is not guaranteed or endorsed by the publisher.

References

Albo, A., Flores, Y. V., Hu, Q., and Reno, J. L. (2019). Split-well direct-phonon terahertz quantum cascade lasers. *Appl. Phys. Lett.* 114, 1911021–1911025. doi:10.1063/1.5089854

Amanti, M. I., Fischer, M., Scalari, G., Beck, M., and Faist, J. (2009). Low-divergence single-mode terahertz quantum cascade laser. *Nat. Photonics* 3, 586–590. doi:10.1038/nphoton.2009.168

Barbieri, S., Alton, J., Beere, H. E., Fowler, J., Linfield, E. H., and Ritchie, D. A. (2004). 2.9 THz quantum cascade lasers operating up to 70K in continuous wave. *Appl. Phys. Lett.* 85, 1674–1676. doi:10.1063/1.1784874

Benz, A., Deutsch, Ch, Fasching, G., Unterrainer, K., Andrews, A. M., Klang, P., et al. (2009). Active photonic crystal terahertz laser. *Opt. Express* 17, 941–946. doi:10.1364/oe.17.000941

Bosco, L., Franckie, M., Scalari, G., Beck, M., Wacker, A., and Faist, J. (2019). Thermoelectrically cooled THz quantum cascade laser operating up to 210 K. *Appl. Phys. Lett.* 115. 0106011–0106015. doi:10.1063/1.5110305

Brandstetter, M., Deutsch, C., Krall, M., Detz, H., MacFarland, D. C., Zederbauer, T., et al. (2013). High power terahertz quantum cascade lasers with symmetric wafer bonded active regions. *Appl. Phys. Lett.* 103, 1711131–1711135. doi:10.1063/1.4826943

Chassagneux, Y., Palomo, J., Colombelli, R., Barbieri, S., Dhillon, S., Sirtori, C., et al. (2007). Low threshold THz QC lasers with thin core regions. *Electron. Lett.* 43, 285–286. doi:10.1049/el:20073842

Chen, Z., Liu, A., Chang, D., Dhillon, S., Razeghi, M., and Wang, F. (2024). Combined resonant tunneling and rate equation modeling of terahertz quantum cascade lasers. *J. Appl. Phys.* 135 (11), 115703. doi:10.1063/5.0198059

Curwen, C. A., Addamane, S. J., Reno, J. L., Shahili, M., Kawamura, J. H., Briggs, R. M., et al. (2021). Thin THz QCL active regions for improved continuous-wave operating temperature. *AIP Adv.* 11, 125018. doi:10.1063/5.0071953

Fathololoumi, S., Dupont, E., Chan, W. I., Wasilewski, Z. R., Laframboise, S. R., Ban, D., et al. (2012). Terahertz quantum cascade lasers operating up to 200 K with optimized oscillator strength and improved injection tunneling. *Opt. Express* 20, 3866–3876. doi:10.1364/oe.20.003866

Gao, L., Feng, C., and Zhao, X. (2023). Recent developments in terahertz quantum cascade lasers for practical applications. *Nanotechnol. Rev.* 12 (1), 20230115. doi:10.1515/ntrev-2023-0115

Gmachl, C., Capasso, F., Sivco, D. L., and Cho, A. Y. (2001). Recent progress in quantum cascade lasers and applications. *Rep. Prog. Phys.* 64, 1533–1601. doi:10.1088/0034-4885/64/11/204

Han, Y. J., Li, L. H., Zhu, J., Valavanis, A., Freeman, J. R., Chen, L., et al. (2018). Silver-based surface plasmon waveguide for terahertz quantum cascade lasers. *Opt. Express* 26, 3814–3827. doi:10.1364/oe.26.003814

Hempel, M., Röben, B., Schrottke, L., Hübers, H. W., Grahn, H. T., and Grahn, H. T. (2016). Fast continuous tuning of terahertz quantum-cascade lasers by rear-facet illumination. *Appl. Phys. Lett.* 108, 1911061–1911065. doi:10.1063/1.4949528

Jenichen, B., Hey, R., Wassermeier, M., and Ploog, K. (1997). Investigation of the interface roughness of GaAs single quantum wells by X-ray diffractometry, reflectivity and diffuse scattering. *Il Nuovo Cimento D.* 19, 429–438. doi:10.1007/bf03041002

Jirauschek, C. (2010). Monte Carlo study of carrier-light coupling in terahertz quantum cascade lasers. *Appl. Phys. Lett.* 96, 011103-1–011103–3. doi:10.1063/1.3284523

Kainz, M. A., Schönhuber, S., Andrews, A. M., Detz, H., Limbacher, B., Strasser, G., et al. (2018). Barrier height tuning of terahertz quantum cascade lasers for high-temperature operation. *ACS Photonics* 5, 4687–4693. doi:10.1021/acsphotonics.8b01280

Kaur, H., Sharma, R., Laurent, T., Torres, J., Nouvel, P., Palermo, C., et al. (2022). Transport characteristics of AlGaN/GaN structures for amplification of terahertz radiations. *Appl. Phys. A* 128, 144. doi:10.1007/s00339-022-05284-8

Khalatpour, A., Paulsen, A. K., Deimert, C., Wasilewski, Z. R., and Hu, Q. (2021). High power portable terahertz laser systems. *Nat. Photonics* 15, 16–20. doi:10.1038/s41566-020-00707-5

Khalatpour, A., Tam, M. C., Addamane, S. J., Reno, J., Wasilewski, Z., and Hu, Q. (2023). Enhanced operating temperature in terahertz quantum cascade lasers based on direct phonon depopulation. *Appl. Phys. Lett.* 122, 161101. doi:10.1063/5.0144705

Kohen, S., Williams, B. S., and Hu, Q. (2005). Electromagnetic modeling of terahertz quantum cascade laser waveguides and resonators. *J. Appl. Phys.* 97, 053106. doi:10.1063/1.1855394

Kruger, O., Kreutzmann, S., Prasai, D., Wienold, M., Sharma, R., Pittroff, W., et al. (2013). Epitaxial-side mounting of terahertz quantum-cascade lasers for improved heat management. *IEEE Photonics Technol. Lett.* 25, 1570–1573. doi:10.1109/lpt.2013.2271323

Kumar, S., Williams, B. S., Qin, Q., Lee, A. W. M., Hu, Q., and Reno, J. L. (2007). Surface-emitting distributed feedback terahertz quantum-cascade lasers in metal-metal waveguides. *Opt. Express* 15, 113–128. doi:10.1364/oe.15.000113

Lee, A. W. M., Williams, B. S., Kumar, S., Hu, Q., and Reno, J. L. (2010). Tunable terahertz quantum cascade lasers with external gratings. *Opt. Lett.* 35, 910–912. doi:10.1364/ol.35.000910

Levy, S., Gower, N. L., Piperno, S., Addamane, S. J., Reno, J. L., and Albo, A. (2024). Analyzing the effect of doping concentration in split-well resonant-phonon terahertz quantum cascade lasers. *Opt. Express* 32, 12040–12053. doi:10.1364/oe.515419

Li, L., Chen, L., Zhu, J., Freeman, J., Dean, P., Valavanis, A., et al. (2014). Terahertz quantum cascade lasers with 1 W output powers. *Electron. Lett.* 50, 309–311. doi:10.1049/el.2013.4035

Li, L. H., Chen, L., Freeman, J. R., Salih, M., Dean, P., Davies, A. G., et al. (2017). Multi-Watt high-power THz frequency quantum cascade lasers. *Electron. Lett.* 53, 799–800. doi:10.1049/el.2017.0662

Li, W., Li, Y., Ma, Y., Xu, Y., Liu, J., Zhuo, N., et al. (2022). Continuous-wave terahertz quantum cascade laser based on a hybrid bound to bound quantum design. *Front. Photonics* 3, 1071879. doi:10.3389/fphot.2022.1071879

Lu, S. L., Schrottke, L., Teitsworth, S. W., Hey, R., and Grahn, H. T. (2006). Formation of electric field domains in GaAs/AlGaAs quantum cascade laser structures. *Phys. Rev. B* 73, 0333111–0333114. doi:10.1103/PhysRevB.73.033311

Lü, X., Röben, B., Schrottke, L., Biermann, K., and Grahn, H. T. (2021). Correlation between frequency and location on the wafer for terahertz quantum-cascade lasers. *Semicond. Sci. Technol.* 36, 035012. 0350121–0350126. doi:10.1088/1361-6641/abdd4b

Mahler, L., Tredicucci, A., Beltram, F., Beere, H. E., and Ritchie, D. A. (2010). Tuning a distributed feedback laser with a coupled microcavity. *Opt. Express* 18, 19185–19191. doi:10.1364/oe.18.019185

Qin, Q., Williams, B. S., Kumar, S., Reno, J. L., and Hu, Q. (2009). Tuning a terahertz wire laser. *Nat. Photonics* 3, 732–737. doi:10.1038/nphoton.2009.218

Röben, B., Lü, X., Biermann, K., Schrottke, L., and Grahn, H. T. (2019). Terahertz quantum-cascade lasers for high-resolution spectroscopy of sharp absorption lines. *J. Appl. Phys.* 125, 1516131–1516137. doi:10.1063/1.5079701

Röben, B., Lü, X., Schrottke, L., Biermann, K., and Grahn, H. T. (2021). Effective group dispersion of terahertz quantum-cascade lasers. *J. Phys. D. Appl. Phys.* 54, 0251101–0251110. doi:10.1088/1361-6463/abbde3

Salih, M., Dean, P., Valavanis, A., Khanna, S. P., Li, L. H., Cunningham, J. E., et al. (2013). Terahertz quantum cascade lasers with thin resonant-phonon depopulation active regions and surface-plasmon waveguides. *J. Appl. Phys.* 113, 1131101–1131105. doi:10.1063/1.4795606

Schrottke, L., Wienold, M., Giehler, M., Hey, R., and Grahn, H. T. (2010). Analysis of the slope efficiency for terahertz quantum-cascade lasers. *J. Appl. Phys.* 108, 1031081–1031086. doi:10.1063/1.3511470

Sharma, R., Kaur, H., and Singh, M. (2021). Recent advances of efficient design of terahertz quantum-cascade lasers. *Plasmonics* 16, 449–461. doi:10.1007/s11468-020-01295-4

Sharma, R., Schrottke, L., Wienold, M., Biermann, K., Hey, R., and Grahn, H. T. (2011). Effect of stimulated emission on the transport characteristics of terahertz quantum-cascade lasers. *Appl. Phys. Lett.* 99, 1511161–1511163. doi:10.1063/1.3653262

Sharma, R., Schrottke, L., Wienold, M., Tahraoui, A., Biermann, K., and Grahn, H. T. (2013). Influence of post-growth rapid thermal annealing on the transport and lasing characteristics of terahertz quantum-cascade laser. *J. Phys. D. Appl. Phys.* 46, 3051071–3051075. doi:10.1088/0022-3727/46/30/305107

Sirtori, C., Capasso, F., Faist, J., Hutchinson, A. L., Sivco, D. L., and Cho, A. Y. (1998). Resonant tunneling in quantum cascade lasers. *IEEE J. Quantum Electron* 34, 1722–1729. doi:10.1109/3.709589

Strupiechonski, E., Grassani, D., Fowler, D., Julien, F. H., Khanna, S. P., Li, L., et al. (2011). Vertical subwavelength mode confinement in terahertz and mid-infrared quantum cascade lasers. *Appl. Phys. Lett.* 98, 101102–101103. doi:10.1063/1.3560980

Terazzi, R., and Faist, J. (2010). A density matrix model of transport and radiation in quantum cascade lasers. *New J. Phys.* 12, 033045. 0330451-03304510. doi:10.1088/1367-2630/12/3/033045

Vitiello, M. S., Consolino, L., Bartalini, S., Taschin, A., Tredicucci, A., Inguscio, M., et al. (2012). Quantum-limited frequency fluctuations in a terahertz laser. *Nat. Photonics* 6, 525–528. doi:10.1038/nphoton.2012.145

Wienold, M., Röben, B., Schrottke, L., Sharma, R., Tahraoui, A., Biermann, K., et al. (2014). High-temperature, continuous-wave operation of terahertz quantum-cascade lasers with metal-metal waveguides and third-order distributed feedback. *Opt. Express* 22, 3334–3348. doi:10.1364/oe.22.003334

Wienold, M., Schrottke, L., Giehler, M., Hey, R., Anders, W., and Grahn, H. T. (2010). Low-threshold terahertz quantum-cascade lasers based on GaAs/Al0.25Ga0.75As heterostructures. *Appl. Phys. Lett.* 97. 0711131-0711133. doi:10.1063/1.3480406

Wienold, M., Schrottke, L., Giehler, M., Hey, R., and Grahn, H. T. (2011). Nonlinear transport in quantum-cascade lasers: the role of electric-field domain formation for the laser characteristics. *J. Appl. Phys.* 109, 0731121–0731126. doi:10.1063/1.3573504

Wienold, M., Tahraoui, A., Schrottke, L., Sharma, R., Lü, X., Biermann, K., et al. (2012). Lateral distributed-feedback gratings for single-mode, high-power terahertz quantum-cascade lasers. *Opt. Express* 20, 11207–11217. doi:10.1364/oe.20.011207

Williams, B. S. (2007). Terahertz quantum-cascade lasers. *Nat. Photonics* 1, 517–525. doi:10.1038/nphoton.2007.166

Williams, B. S., Kumar, S., Hu, Q., and Reno, J. L. (2006). High-power terahertz quantum-cascade lasers. *Electron Lett.* 42, 89–91. doi:10.1049/el:20063921

Xu, J., Hensley, J. M., Fenner, D. B., Green, R. P., Mahler, L., Tredicucci, A., et al. (2007). Tunable terahertz quantum cascade lasers with an external cavity. *Appl. Phys. Lett.* 91, 1211041–1211043. doi:10.1063/1.2786587